Leaf-inspired hierarchical porous CdS/Au/N-TiO₂ heterostructures for visible light photocatalytic hydrogen evolution

Han Zhou [a,b], Liang Ding [a], Tongxiang Fan [a,*], Jian Ding [a], Di Zhang [a], Qixin Guo [c]

[a] State Key Laboratory of Metal Matrix Composites, Department of Materials science and Engineering, Shanghai Jiaotong University, Shanghai 200240, China
[b] Max Planck Institute of Colloids and Interfaces, Department of Colloid Chemistry, Research Campus Golm, 14424 Potsdam, Germany
[c] Department of Electrical and Electronic Engineering, Saga University, Saga 840-8502, Japan

ABSTRACT

Photosynthesis has been for many years a fascinating source of inspiration for the development of model systems able to achieve efficient solar-to-chemical transduction. In the hot field of artificial photosynthesis, considerable progress has been made toward converting solar energy into the carbon-free fuel "hydrogen" through photocatalytic water splitting. Here, we report a promising photocatalytic system with both desirable morphology and suitable band-gap configuration for efficient visible light water splitting. Such photocatalyst is realized by the inspiration from leaf's morphology and photosynthesis basic mechanism – Z scheme reaction. The unique architectures – hierarchical macro/mesoporous morphology of natural leaves are retained in the man-made systems to enhance overall light harvesting and to offer more absorption and reaction sites for the catalytic reactions. The photocatalytic modules – CdS(shell)/Au(core)/N-TiO₂ heterostructures are served as a prototype here to demonstrate this concept, in which N-TiO₂ and CdS serve as PS II and PS I, respectively, while Au acts as the electron transfer mediator, contributing to the enhancement of electron hole separation and interfacial charge transfer. The CdS(shell)/Au(core)/N-TiO₂ heterostructures are obtained *via* a two-step photodeposition method. The particle sizes of Au cores, the contents and thicknesses of CdS shells are controlled by varying the synthetic parameters (*e.g.* irradiation time) to obtain an optimized activity. The H₂ evolution rates of optimized CdS/Au/N-TiO₂ heterostructures are about 2.6 times of N-TiO₂ under UV/visible light, and about 270 times of Au/N-TiO₂ under visible light irradiation. The systems have high visible light harvesting, high hydrogen evolution rate and long electron–hole lifetimes compared with non-incorporated systems. The design of this system is based on both biological morphology and mechanism paradigms, which would provide a proof of concept for the bio-inspired design of artificial photosynthetic system for enhanced photocatalytic performance.

© 2013 Elsevier B.V. All rights reserved.

1. Introduction

Providing abundant and clean renewable energy sources is one of the key technological challenges facing mankind [1]. One alternative energy source of particular interest is solar energy. The conversion of solar energy into chemicals to generate "solar fuels" should be the most promising proposition for a long-term solution of the global energy crisis [2,3]. Photosynthesis has been for many years a fascinating source of inspiration for the development of model systems able to achieve efficient solar-to-chemical transduction [4]. In the hot field of artificial photosynthesis, considerable progress has been made toward converting solar energy into the carbon-free fuel "hydrogen" through photocatalytic water splitting [5–7]. In general, two strategies are being used for enhanced efficiency. One is morphology control by the construction of nano- or mesostructured materials (*e.g.* nanosheets, nanowires, nanotubes, mesoporous structures, hollow structures, and hierarchical architectures) with large surface areas and abundant surface states for enhanced light harvesting, more absorption/reaction sites and fast separation of photogenerated electron–hole pairs [8–13]. The other approach is composition adjustment by energy band engineering (*e.g.* doping, sensitization, *etc.*) to absorb more visible light or through heterojunctions to facilitate efficient transfer of photogenerated charge carriers between interfaces [14–18]. A promising catalyst for efficient water splitting would need to exhibit both desirable morphology as well as suitable band-gap configuration for improved performances. The application of concepts derived from natural photosynthesis is highly attractive for the development of novel artificial photosynthetic systems.

Recently, we demonstrated that the whole hierarchical morphology of natural leaves strongly favors light harvesting [19]. Accordingly, we constructed artificial inorganic leaves (Pt/N-TiO₂)
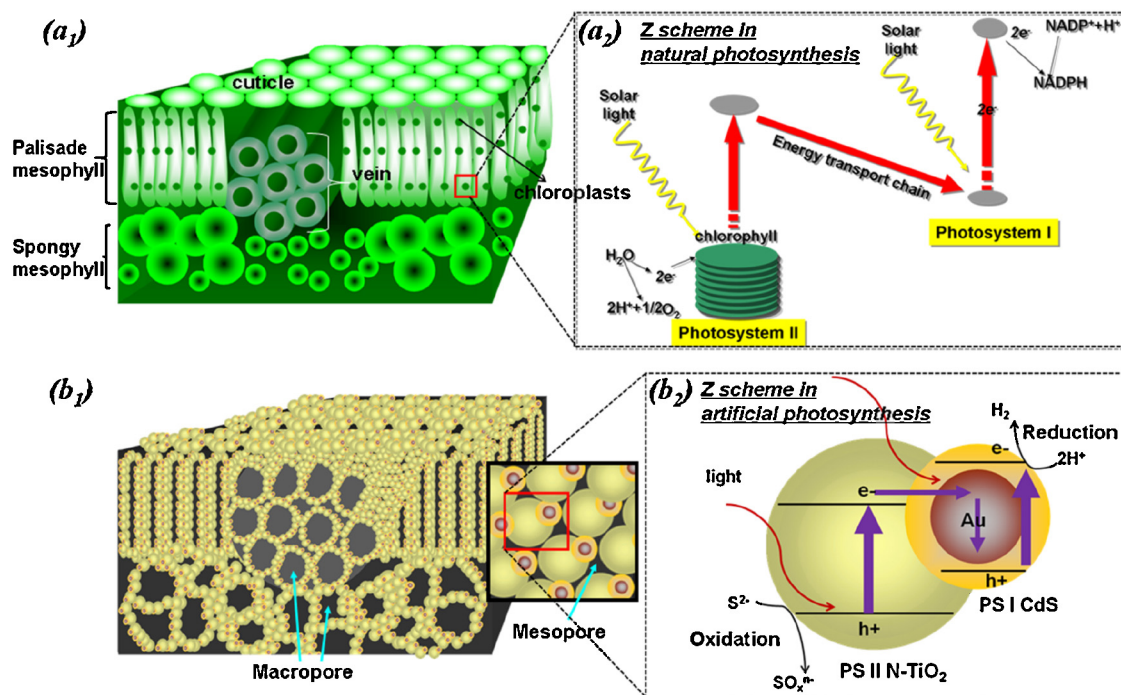
Fig. 1. Schematic illustrations of (a_1) the cross section of leaf's hierarchical morphologies. (a_2) Z scheme in natural photosynthesis. (b_1) The cross section of the hierarchical macro/mesoporous heterostructures in the multicomponent artificial systems. (b_2) Z scheme in artificial photosynthesis.

by replicating the hierarchical structure of natural leaves and self-doping of nitrogen in metal oxides for enhanced light harvesting and efficient photocatalytic activities [19,20]. The research indicated that the design of artificial systems based on biological morphology paradigms could be an effective fascinating pathway for morphology optimization. However, though doping of TiO$_2$ with nonmetallic (*e.g.* N) [21,22] elements extends its optical absorption to the visible region, the utilization of visible light spectra is still rather low (λ >420 nm). Furthermore, doping usually comes with accelerated charge recombination and lower stability. Thus, the extension of such strategy to a system with more efficient visible light response, lower charge recombination possibility and longer electron-hole lifetimes is of high significance.

The Z-scheme system in the natural photosynthesis of green leaves provides us inspirations to these problems [23]. The Z-scheme shows the pathway of electron transfer from water to NADP$^+$ *via* a two-step photon-excitation process to realize water oxidation into oxygen in photosystem II (PS II) and water reduction into NADPH in photosystem I (PS I), respectively (Fig. 1a$_2$). Theoretically, by taking advantage of a combination of PS I and PS II, the probabilities of charge recombination would be decreased significantly, thus resulting in more electrons available to participate in the reduction step of the reaction. Z-scheme water splitting was first introduced by Bard in 1979 [24]. Since then many efforts have been made to construct such systems, focusing on the development of new materials and effective electron relays [25–35] including Pt–WO$_3$/Pt–SrTiO$_3$ (Cr–Ta-doped), Pt–SrTiO$_3$/Rh–BiVO$_4$, RuO$_2$–TaON/Pt–TaON, etc with Fe^{2+}/Fe^{3+} or I$^-$/IO$_3^-$ or Br$^-$/Br$_2$ as redox mediators [26,32] and two component heterostructures such as Cr–In$_2$O$_3$/Cr–Ba$_2$In$_2$O$_3$, ZnO/CdS, etc. [33] and three component heterostructures such as AgBr–Ag–Bi$_2$WO$_6$, CdS/Au/TiO$_2$, AgBr–Ag–TiO$_2$, etc. [35]. However, to our knowledge, there have been few reports focused on the morphological optimization of Z scheme systems.

In the present work, we report a promising photocatalytic system with both favorable morphology and components for efficient visible light water splitting. Such photocatalyst would be realized

by mimicking leaf's hierarchical porous morphology as well as photosynthesis basic mechanisms (Z scheme). The unique architectures – hierarchical macro/mesoporous morphology of natural leaves would be retained in the man-made systems to enhance overall light harvesting and to offer more absorption and reaction sites for the catalytic reactions. The photocatalytic modules – CdS(shell)/Au(core)/N-TiO$_2$ heterostructures are served as a prototype here to demonstrate this concept, in which N-TiO$_2$ and CdS serve as PS II and PS I, respectively, while Au acts as the electron transfer mediator, contributing to the enhancement of electron hole separation and interfacial charge transfer. The contents of CdS shells are controlled to obtain an optimized activity. The photocatalyst is expected to have high visible light harvesting, high hydrogen evolution rate, and long electron-hole lifetimes compared with non-incorporated systems. The design of this system is based on both biological morphology and mechanism paradigms, which would provide a proof of concept for the bio-inspired design of artificial photosynthetic system for enhanced performance.

2. Experimental

2.1. Synthesis

The hierarchical porous CdS/Au/N-doped TiO$_2$ three-component heterostructures were prepared by the following three steps: in a typical procedure, hierarchical porous N-doped TiO$_2$ were first synthesized using *Cherry blossom* leaves as biotemplates according to our previous report [20]. Au nanoparticles were deposited on N-doped TiO$_2$ particles by a photodeposition method. Au nanoparticles with a mean size of 5 nm were loaded on N-doped TiO$_2$ by irradiating N-doped TiO$_2$ materials in 1 vol% aqueous methanol containing 1 wt% (based on N-doped TiO$_2$) HAuCl$_4$·4H$_2$O. The reaction mixture was stirred in an Ar atmosphere and irradiated under a 750 W Xenon lamp (integrated intensity: 38.1 mW/cm^2) for 5 min. After irradiation, the samples were centrifuged, washed with DI water for four times, and dried under vacuum at 40 °C. CdS nanoparticles were deposited on
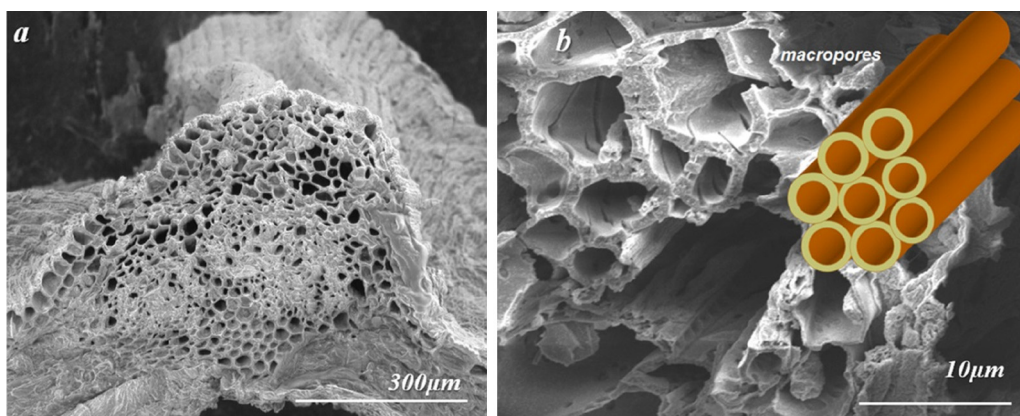
Fig. 2. (a) FESEM image of the cross-section of the vein architecture of Cherry blossom leaf. (b) TEM image of a granum – the layered nanostructure of thylakoid membranes, with the inset as a schematic illustration.

Au/N-doped TiO$_2$ through photodeposition method. Au/N-TiO$_2$ particles (100 mg) ethanol aqueous suspension (50 ml; $v{:}v = 3{:}2$) containing S$_8$ (30 mg) and Cd(NO$_3$)$_2$·4H$_2$O (450 mg) was bubbled with argon for 30 min in dark. Irradiation was carried out for a given period of time (0–5 h) with Xenon lamp at room temperature to vary the contents of CdS. Then products were centrifuged with water and ethanol, and dried at 50 °C in air. Pt nanoparticles (1 wt%) were also loaded on the prepared samples by a photodeposition method as cocatalyst for water-splitting. H$_2$PtCl$_6$·6H$_2$O was added to the Na$_2$S (0.25 M)–Na$_2$SO$_3$ (0.35 M) mixed solution containing the photocatalyst. The resulting suspension was then irradiated with Xenon lamp for 1 h. Finally, the Pt-deposited photocatalyst was obtained after centrifugation.

2.2. Characterization

Field emission scanning electron microscope (FESEM) observations were performed with a FEI SIRION 200 instrument operated at 5 kV. FESEM samples were sputtered with gold. Transmission electron microscopy (TEM) and high-resolution transmission electron microscopy (HRTEM) images were conducted on a JEOL JEM-2010 instrument operated at an accelerating voltage of 200 kV (with energy dispersive X-ray spectroscopy, EDS, Oxford INCA) and a JEOL JEM-2100F instrument operated at an accelerating voltage of 200 kV, respectively. UV–vis absorption spectroscopy of all of the samples was recorded using a Varian Cary UV–vis–NIR spectrophotometer in the spectral range 200–800 nm. 0.25 g of each sample was pressed between two pieces of quartz glass within the 3 × 3 cm area to cover the aperture through which the excitation light passed. A BaSO$_4$ plate was used as the basic line for the spectra. The crystal phase of the samples was examined by X-ray diffraction (XRD) measurements on a Bruker-AXS X-ray diffractometer system with Cu Ka radiation at 40 kV and 100 mA. The pore-size distributions were evaluated by nitrogen adsorption measurements, operated at 77 K on a Micromeritics ASAP 2010 adsorption analyzer. The pore-sizes and distribution curves were derived from the adsorption isotherm by employing the Barrett–Joyner–Halenda (BJH) method. Au and CdS contents *versus* TiO$_2$ were measured on an inductively Coupled Plasma Optical Emission Spectrometer (ICP-OES) (iCAP6300, Thermo Electron Corporation). Steady-state and Time-Resolved Fluorescence Spectrofluorometer (PTI, QM/TM/IM) was used to get samples' transient spectra (TRS) in Ar at room temperature. The excitation wavelength λ_{ex} is 390 nm. Raw decay data presented as logarithm of photon counts versus time were analyzed with data analysis software of PicoQuant GmbH. The decay times were extracted by means of a reconvolution fit based on a double or triple exponential model. Considering that $I_{PL}(t) =$

$\sum_{i=1}^{i=n} a_i e^{-t/\tau_i}$ where τ_i is the lifetime and a_i is the amplitude of the ith component, the intensity-averaged fluorescence lifetime τ was calculated as $\tau = \frac{\sum_{i=1}^{i=n} a_i \tau_i^2}{\sum_{i=1}^{i=n} a_i \tau_i}$

2.3. Photocatalytic H$_2$ evolution experiments

Irradiation was performed in a closed gas circulation system at 30 °C using a 750 W Xe arc lamp with a measured irradiance of 38.1 mW/cm^2 at the glass flask surface. A cutoff filter ($\lambda > 400$ nm) was employed for visible-light irradiation. The photocatalytic reaction was performed in a quartz flask containing CdS/Au/N-TiO$_2$ catalysts (100 mg) and Na$_2$S (0.25 M)–Na$_2$SO$_3$ (0.35 M) mixed solution (100 ml), Then the flask was evacuated and purged four times with argon gas, and the stirred mixture was then irradiated for 5 h. Gas samples were periodically analyzed with a Varian gas chromatograph (HXSP, GC-950) employing a Supelco molecular 60/80 sieve 5A column with Ar as the carrier gas and a thermal conductivity detector (TCD).

3. Results and discussion

Here *Cherry blossom* leaf, a typical dicotyledon leaf is chosen as a model. As shown in the cross-section (Fig. 1a$_1$), a leaf is mainly composed of veins, palisade mesophyll, and spongy mesophyll layers arranged between two layers of epidermal cells from a tissue scale. The cross-section of the veins indicates highly porous architectures (Fig. 2a). Light that enters leaf venation architectures becomes highly scattered and increases light absorption. The internal structure of an individual mesophyll cell contains a number of chloroplasts. Each chloroplast contains nanolayered (only several nanometers) thylakoids stacks (granum) as shown in Fig. S1a. Such stacked nanolayered three-dimensional lamellar structures with high surface areas are favorable for the efficient interaction between photosynthetic pigments and sunlight. Based on the hierarchical porous morphology of natural leaf, N-doped TiO$_2$ replicas are obtained *via* a two-step infiltration process with leaves as templates, as demonstrated by our previous research [20]. The replicas inherit the hierarchical morphologies of the natural leaf at macro-, micro-, and nanoscales including a porous framework of veins (Fig. 2b) and nanolayered lamellar structures of granums in chloroplast (Fig. S1b). Such hierarchical porous morphologies endow them with high specific surface areas and macropore/mesopore architectures (Fig. 2b and Fig. S2).
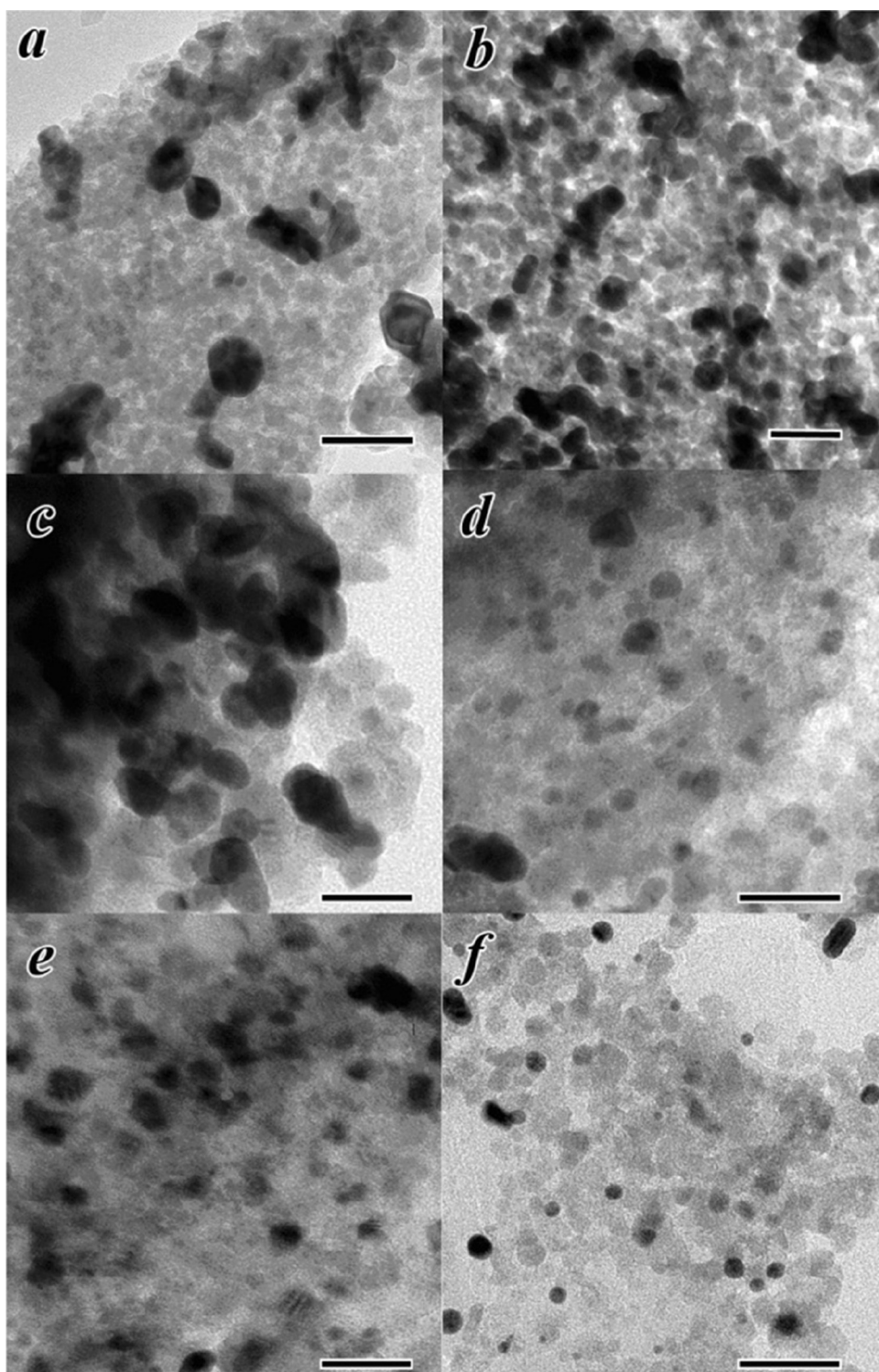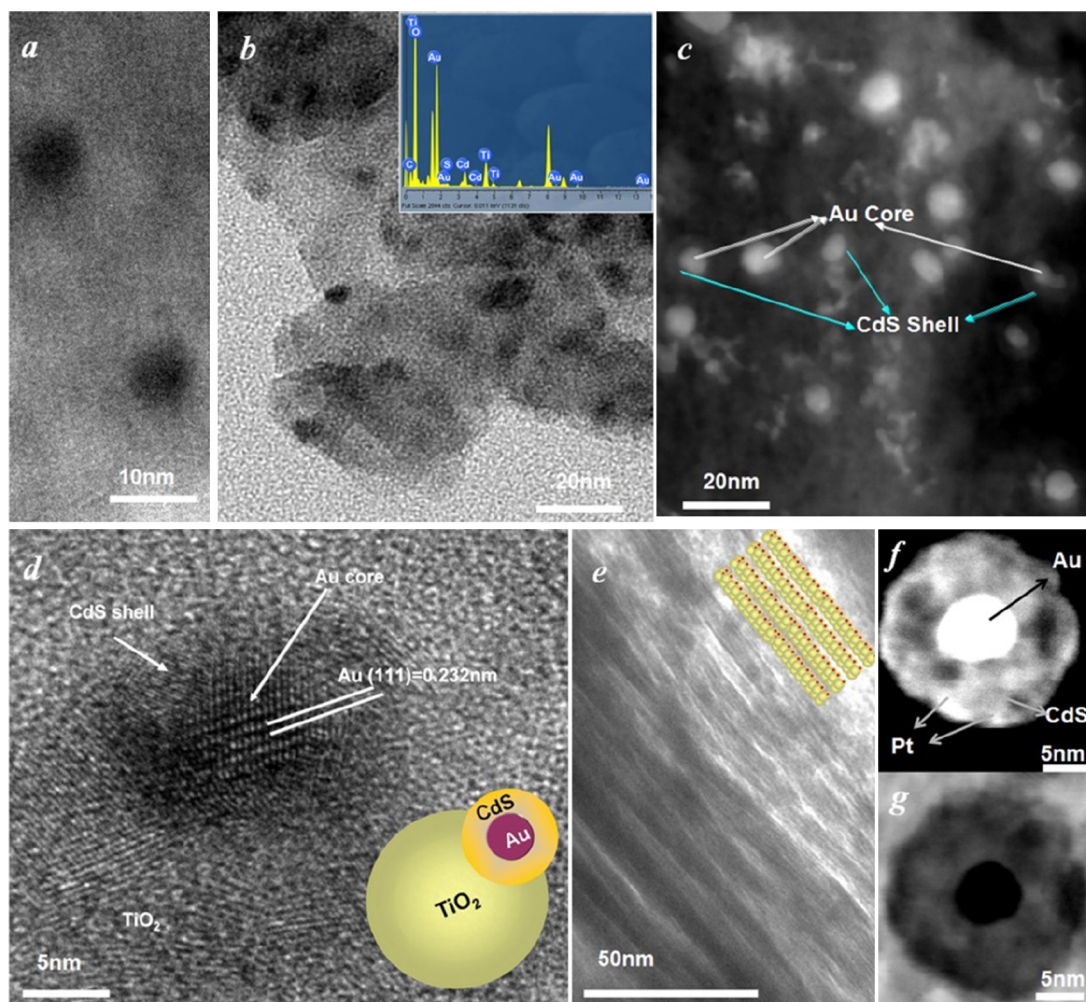
Fig. 3. TEM images of Au nanoparticles loaded on N-TiO$_2$ by photodeposition under different conditions (a) irradiated in 20 vol% aqueous methanol for 1 h (b) irradiated in 5 vol% aqueous methanol for 5 min. (c) Irradiated in 5 vol% aqueous methanol for 4 min. (d) Irradiated in 5 vol% aqueous methanol for 2 min. (e) Irradiated in 2 vol% aqueous methanol for 5 min. (c) Irradiated in 2 vol% aqueous methanol for 4 min. The irradiation distance of (a) is 30 cm, while that of others is 10 cm. Scale bar: 20 nm.

Photodeposition of Au nanoparticles on resulting N-TiO$_2$ was carried out under UV light irradiation after adsorption in HAuCl$_4$ aqueous solution. The sizes and distribution of Au nanoparticles loaded on hierarchical porous N-TiO$_2$ could be controlled by changing the irradiation time, irradiation distance and the concentration of methanol in HAuCl$_4$ solution. When loaded in relatively high concentration of methanol, the Au particles prefer to cluster together (Fig. 3a–d). The particle distribution is not homogeneous. Many particles are agglomerated. This indicates that these particles nucleated in solution. That shows that sacrificial agents do raise the charge carrier concentrations in the nanoparticles. In the meantime, with the increase of the irradiation time, the average diameters of Au particles increase (Fig. 3). Overall, the results show that Au nanoparticle sizes depend on the experimental conditions

Fig. 4. TEM images of (a) Au nanoparticles loaded on N-TiO$_2$. (b) CdS/Au/N-TiO$_2$ heterostructures at low magnification, with the inset of the corresponding EDS spectra. The irradiation time for the photodeposition of CdS is 0.5 h. (c) HAADF-STEM image of CdS/Au/N-TiO$_2$ heterostructures. (d) HRTEM image of CdS/Au/N-TiO$_2$ heterostructures. It can be seen that Au–CdS core–shell structure was formed on the N-TiO$_2$, with the inset of the schematic illustration. (e) TEM image of nanolayered structures of CdS/Au/N-TiO$_2$, with the inset of the schematic illustration. (f) HAADF-STEM image of Pt/CdS/Au/N-TiO$_2$ in dark field. Small Pt nanoparticles were observed on the CdS shell as bright spots. (g) HAADF-STEM image of Pt/CdS/Au/N-TiO$_2$ in bright field.

of deposition. We controlled the Au particle size by varying these parameters, and the as-obtained Au nanoparticle is about 5 nm with relatively uniform dispersion in N-TiO$_2$ substrate (Fig. 4a). For the photodeposition of CdS, S$_8$ is strongly and selectively adsorbed on the Au surface of Au/N-TiO$_2$ first due to the specific strong S–Au interaction [36]. The electrons accumulated in Au reduce S selectively adsorbed to S^{2-} ions. The reaction of S^{2-} ions and Cd^{2+} ions yields CdS on the Au surface *via* an ionic route to form Au(core)–CdS(shell) heterostructures (Fig. 4b) [37]. Fig. 4c is a HAADF-STEM image of CdS(shell)/Au(core)/N-TiO$_2$, clearly revealing the existence of core–shell structures. Fig. 4d is a HRTEM image of CdS(shell)/Au(core)/N-TiO$_2$. The lattice spacings of the core determined to be 0.232 nm, are in agreement with the values for the Au (1 1 1) plane. From the TEM image, the average thickness of CdS shell is about 4 nm with the irradiation time for the deposition of 1 h. The thickness of CdS layer could be controlled by the irradiation time (Fig. S3). After photodeposition of Au and CdS particles sequentially, the as-obtained three component systems still retain the nanolayered structures derived from the thylakoids stacks in chloroplast (Fig. 4e).

UV–vis spectra are used to compare their light harvesting abilities (Fig. 5). Compared with TiO$_2$ nanoparticles synthesized without templates, the band-gap-absorption onset of the
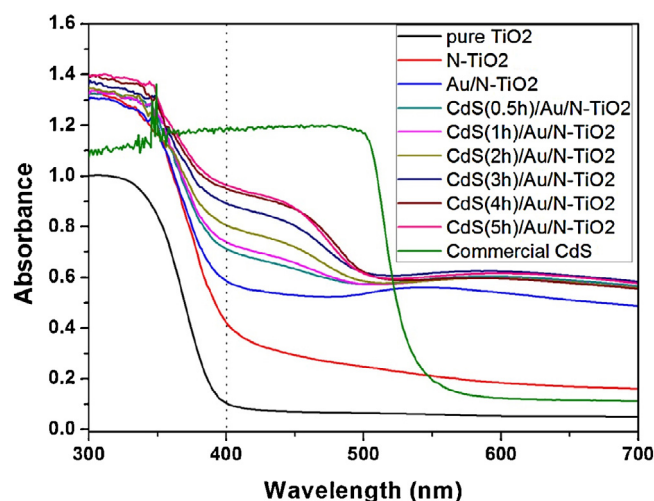
Fig. 5. UV–vis absorption spectra of a series of the samples.

Table 1
The contents of Au and CdS *versus* N-TiO$_2$ measured by inductively coupled plasma optical emission spectrometer (ICP).

Samples	CdS(0.5 h)/Au/N-TiO$_2$	CdS(1 h)/Au/N-TiO$_2$	CdS(2 h)/Au/N-TiO$_2$	CdS(3 h)/Au/N-TiO$_2$	CdS(4 h)/Au/N-TiO$_2$
Au:N-TiO$_2$ (wt%)	0.45	0.41	0.41	0.34	0.44
CdS[a]:N-TiO$_2$ (wt%)	2.71	3.04	3.87	5.19	6.71

[a] The contents of CdS were calculated based on the contents of Cd and S.

hierarchical porous N-TiO$_2$ derived from leaf templates shows a red-shift. This is caused by the self-doping of N with weight contents of about 0.9–1.5% [20]. Compared with pure N-TiO$_2$, Au/N-TiO$_2$ composite shows a broad peak at 530 nm, corresponding to plasmon resonance (PR) absorption of Au nanoparticles. The peak position and shape are consistent with those of 5 nm Au particles loaded on TiO$_2$ [38]. Addition of CdS resulted in the appearance of an additional absorption band in the visible region, the intensity of which monotonically increased with an increase of CdS content (Table 1). After deposited CdS shell on Au nanoparticles, the PR absorption peak of Au nanoparticles redshifted to ~585 nm and broadened due to the strong electromagnetic coupling of Au and CdS [39]. The shoulder peak at 430 nm of CdS/Au/N-TiO$_2$ heterostructures is due to the absorption of CdS shell. The results demonstrate that CdS shells are successfully covered on the Au cores to form PS I, as evidenced by TEM, UV–vis data and XRD (Fig. S4).

Photocatalytic water splitting for H$_2$ evolution was carried out. Hierarchical porous N-TiO$_2$ evolved H$_2$ up to 13.7 μmol after 5 hr irradiation under UV and visible light (Fig. 6a), the activity of which is much higher than that of P25 and TiO$_2$ synthesized without leaf templates as demonstrated in our previous study [19]. The hierarchical porous morphologies including a high surface area at macroscale, a porous framework at microscale, and an interconnected, nanolayered, 3D construction nanostructure at nanoscale can offer more absorption and reaction sites for the photocatalytic reaction. When 1 wt% Au nanoparticles are directly grown onto the N-TiO$_2$, the hydrogen evolution rate increased. It is known that the Au co-catalyst promotes charge transfer and creates hydrogen desorption sites, leading to higher photocatalytic activity for H$_2$ production [40,41]. Compared to pure N-TiO$_2$ and the Au/N-TiO$_2$ two-component nanojunction, all the CdS/Au/N-TiO$_2$ three-component heterostructures exhibited higher photocatalytic performance (Fig. 6a). Increase of CdS resulted in a progressive increase of the hydrogen evolution rate under UV and visible light irradiation, however, additional increase of the CdS content (*versus* N-TiO$_2$) to 3.87 wt% (Fig. 6c and Table 1) resulted in a decrease of the rate. This is because at higher CdS contents, the Au/N-TiO$_2$ particles are covered by excess amounts of CdS which restrict efficient light harvesting by N-TiO$_2$ (PS II). In the meanwhile, previous study revealed that with the irradiation time increase, the mean CdS particle sizes increase slightly while the band gap (*Eg*) of CdS decrease accordingly because of the size quantization [42]. The reaction yield is a parameter which mainly depends on the CdS shell thickness, nanocrystal size, and is too complex to be precisely controlled. The photocatalyst containing 6.71 wt% CdS (*versus* N-TiO$_2$) yielded the
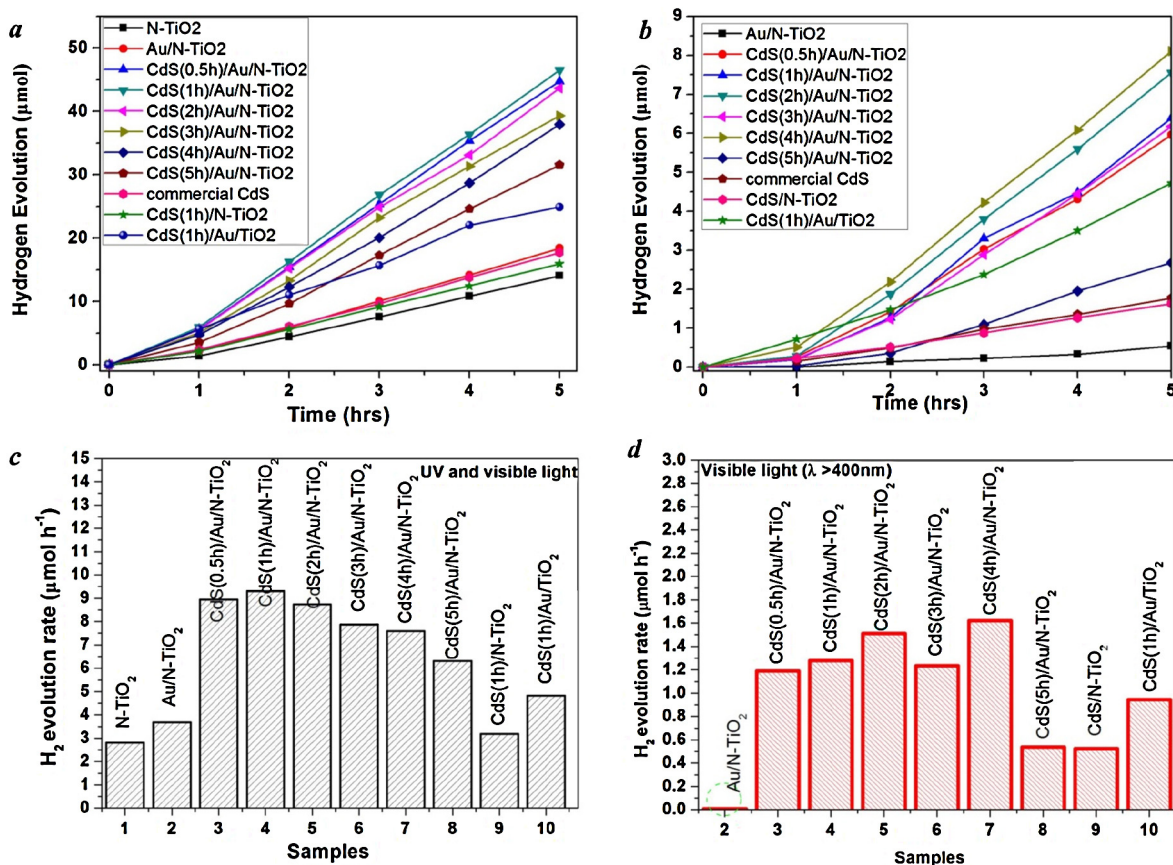
Fig. 6. (a) H$_2$ evolution of the samples under UV and visible light irradiation. (b) H$_2$ evolution of the samples under visible light (λ > 400 nm) irradiation. (c) Calculated H$_2$ evolution rates under UV and visible light irradiation. (d) Calculated H$_2$ evolution rates under visible light irradiation, indicating the probably trend for H$_2$ evolution as a function of the CdS contents.

highest rate of hydrogen evolution under visible light ($\lambda > 400$ nm) irradiation (Fig. 6b). Fig. 6c and d shows the values of H_2 evolution rate as a function of the CdS content in the CdS/Au/N-TiO$_2$ heterostructures. The H_2 evolution rate of optimized CdS/Au/N-TiO$_2$ three-component heterostructures is about 2.6 times of N-TiO$_2$ under UV/visible light irradiation while that is almost 270 times of Au/N-TiO$_2$ under visible light irradiation (Fig. 6c and d). For comparison, we measured CdS/N-TiO$_2$ (non-Au system) under UV–visible light and visible light irradiation, respectively. The H_2 evolutions are lower compared with CdS/Au/N-TiO$_2$ ternary heterojunctions, which demonstrate the advantages of our systems. Furthermore, we prepared CdS/Au/TiO$_2$ (without N-doping) from wood template. XPS data (Fig. S5) show that TiO$_2$ derived from wood template is not N-doped. N$_2$ adsorption–desorption measurement reveals that the TiO$_2$ has comparable surface area with leaf-templated TiO$_2$. Then, we measured their activities under full-arc spectrum and visible light region as shown in Fig. 6. The properties show that CdS/Au/TiO$_2$ (without N-doping) systems have lower activities. The activity of the series of CdS/Au/N-TiO$_2$ heterostructures containing 2.71–6.71 wt% CdS without any cocatalyst (e.g. Pt) is about 2–3 times of pure commercial CdS under UV/visible light irradiation while that of the optimized heterostructure is about 5 times of pure commercial CdS under visible light irradiation (Fig. 6a and b). After loading with 1 wt% Pt cocatalyst, the quantum efficiency (QE) of the optimized heterostructure is ∼3.23% at 420 nm. HAADF-STEM analysis, which easily distinguishes between different materials in a very small dimension, was carried out to verify the presence of Pt nanoparticles on the CdS shell as cocatalyst for water-splitting (Fig. 4f and g). The images clearly show that they are relatively deposited on the CdS shell with a size of 3–5 nm. O$_2$ could not be detected because of the holes left in the valence band of N-TiO$_2$ are consumed for oxidation reaction with the S^{2-} anions as shown in Fig. 1b$_2$.

To better understand the synergistic effects of coupled CdS/Au/N-TiO$_2$ three component heterojunctions on hydrogen evolution, time-resolved fluorescence measurements were carried out (Fig. 7). Fluorescence lifetimes extracted from the decay curves are given in Fig. 7b. N-TiO$_2$ itself has a fluorescence lifetime of about 1.132 ns. When loaded with Au, the fluorescence lifetime of Au/N-TiO$_2$ decreased to 0.968 ns due to the electron transfer from N-TiO$_2$ to Au. In the CdS/Au/N-TiO$_2$ three component heterojunctions, the fluorescence lifetime was reduced to 0.722 ns, indicating the transfer of photoexcited electrons and holes between N-TiO$_2$, Au and CdS exist, which can retard the recombination probability of electron and hole pairs and thus improve its photoactivity proposed in Fig. 1b$_2$. The photocatalytic results are in line with the lifetime measurements. CdS/Au/N-TiO$_2$ has the shortest lifetime which means, the excited electrons and holes are easier to transfer and separated, thus it has the highest activity. Photo-generated electrons in the conduction band of N-TiO$_2$ (PS II) easily flow into Au through the Schottky barrier [37,43], and the holes left in the valence band of N-TiO$_2$ are available for oxidation reaction. Simultaneously, the photo-generated holes in the valence band of CdS (PS I) also easily flow into Au to recombine with the stored electrons, because of the higher Fermi energy levels of noble metal than the valence band level of CdS [37,43], and the electrons left in the conduction band of CdS are available for reduction reaction. Thus, the resulted vectorial photo-generated electrons transfer of N-TiO$_2 \rightarrow$ Au $\rightarrow$ CdS realizes the complete separation of photo-generated holes in the valence band of N-TiO$_2$ and electrons in the conduction band of CdS. This conclusion is also demonstrated by other's previous work [37]. Furthermore, the location of Pt particles could support this claim. As we know, electrons can easily transfer from N-TiO$_2$ to Au with a large work function. Then if the electron transfer from CdS to N-TiO$_2$ rapidly takes place through their contact with Au, Pt should be photodeposited on N-TiO$_2$. However, HAADF-STEM image (Fig. 4f)
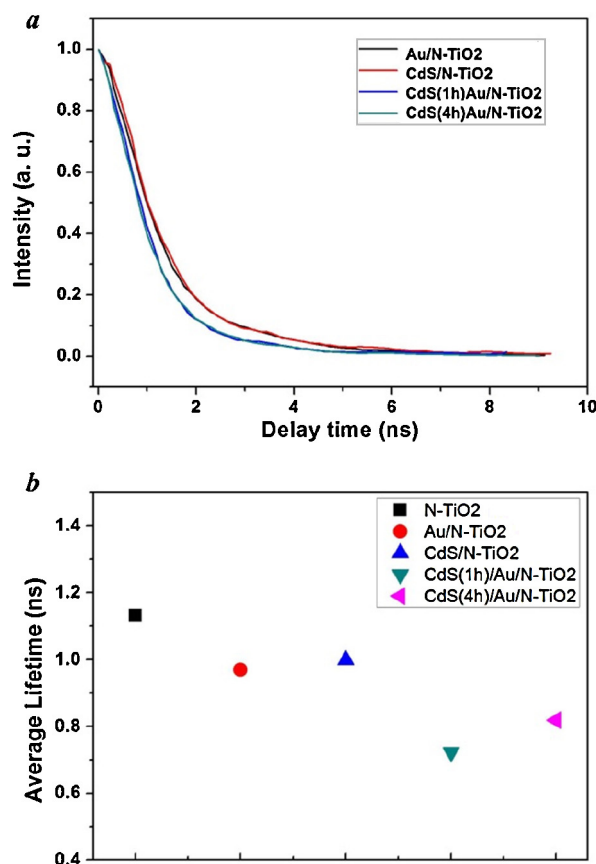

Fig. 7. (a) Fluorescence decay curves of the N-TiO$_2$, Au/N-TiO$_2$ and CdS(1 h)/Au/N-TiO$_2$, CdS(4 h)/Au/N-TiO$_2$. The powder samples were excited by the 390 nm excitation source in Ar at room temperature. The detection wavelength was 450 nm. (b) Fluorescence lifetimes of the samples.

of Pt/CdS/Au/N-TiO$_2$ nanoparticles shows that small Pt nanoparticles were observed on the CdS shell. This finding demonstrates that CdS acts as the reduction sites of CdS/Au/N-TiO$_2$, in the meantime the back electron transfer from CdS to N-TiO$_2$ is a minor path, strongly supporting the vectorial electron transfer. The successful realization of Z-scheme mechanism under the irradiation of UV and visible light led to an exceptional performance in the photocatalytic evolution of H$_2$ via water-splitting. This process is similar with the Z scheme in natural photosynthesis (Fig. 1a$_2$). Furthermore, the electron supply from N-TiO$_2$ to CdS via Au restricts the self-decomposition of CdS due to the oxidation of surface S^{2-} ions by the vb-holes (CdS) [44].

4. Conclusions

Inspired by the photosynthesis of natural leaves, we have put forward a new idea for the construction of efficient photocatalysts by incorporating favorable morphologies and components for visible light photocatalytic hydrogen evolution. The unique architectures-hierarchical macro/mesoporous morphology of natural leaves retained in the synthesized photocatalysts have enhanced the overall light harvesting and offered more absorption and reaction sites for the catalytic reactions. The incorporated photocatalytic modules – CdS(shell)/Au(core)/N-TiO$_2$ heterostructures, have demonstrated to increase visible light catalysis significantly and to prolong electron–hole lifetimes by mimicking Z scheme reactions in photosynthesis. The synergy of desirable morphologies and components contributes to much higher hydrogen evolution rate in the visible light compared with non-incorporated

systems. The contents and thicknesses of CdS shells are controlled to obtain an optimized activity. The H_2 evolution rates of optimized CdS/Au/N-TiO$_2$ three-component heterostructures are about 2.6 times of N-TiO$_2$ under UV/visible light, and about 270 times of Au/N-TiO$_2$ under visible light irradiation. Here, we used leaf as a typical example to demonstrate an effective way for the synthesis of hierarchical porous photocatalytic systems. Indeed, hierarchical constructions on a scale ranging from nanometers to millimeters are characteristic of biological structures and introduce the capacity to answer physical or chemical demands occurring at these different levels. Many of these hierarchical, elaborate structures are barely attainable by man-made materials. This method could be extended to various hierarchical porous biological templates, such as diatoms, radiolarians, pollen grains, sponge and so forth. In the meanwhile, our means represents a versatile approach to a variety of other Z scheme systems with hierarchical porous morphologies for enhanced activities. Nature has provided us huge resources for inspiration [13,45,46], and learning from nature's morphologies and basic mechanisms would be a good starting point for biomimicry, and are expected to be promising for enhanced solar energy harvesting and transduction performances.

Acknowledgments

Appendix A. Supplementary data

Supplementary data associated with this article can be found, in the online version, at http://dx.doi.org/10.1016/j.apcatb.2013.08.025.

References

[1] N.S. Lewis, D.G. Nocera, Proc. Natl. Acad. Sci. USA 103 (2006) 15729–15735.
[2] H. Tong, S. Ouyang, Y. Bi, N. Umezawa, M. Oshikiri, J. Ye, Adv. Mater. 24 (2012) 229–251.
[3] F.E. Osterloh, Chem. Mater. 20 (2008) 35–54.
[4] J. Barber, B. Andersson, Nature 370 (1994) 31–34.
[5] A. Listorti, J. Durrant, J. Barber, Nat. Mater. 8 (2009) 929–930.
[6] H. Zhou, T. Fan, D. Zhang, ChemCatChem 3 (2011) 513–528.
[7] X. Wang, K. Maeda, A. Thomas, K. Takanabe, G. Xin, J.M. Carlsson, K. Domen, M. Antonietti, Nat. Mater. 8 (2009) 76–80.
[8] G.K. Mor, O.K. Varghese, M. Paulose, K. Shankar, C.A. Grimes, Sol. Energy Mater. Sol. Cells 90 (2006) 2011–2075.
[9] X.W. Lou, L.A. Archer, Z.C. Yang, Adv. Mater. 20 (2008) 3987–4019.
[10] C.-J. Liu, U. Burghaus, F. Besenbacher, Z.L. Wang, ACS Nano 4 (2010) 5517–5526.
[11] F. Wang, C. Li, Y. Li, J.C. Yu, Appl. Catal. B, Environ. 119–120 (2012) 267–272.
[12] J.J. Lin, J.X. Shen, R.J. Wang, J.J. Cui, W.J. Zhou, P.G. Hu, D. Liu, H. Liu, J.Y. Wang, R.I. Boughton, Y.Z. Yue, J. Mater. Chem. 21 (2011) 5106–5113.
[13] Z. Schnepp, Angew. Chem. Int. Ed. 52 (2013) 1096–1108.
[14] X. Chen, S. Shen, L. Guo, S.S. Mao, Chem. Rev. 110 (2010) 6503–6570.
[15] Z. Yi, J. Ye, N. Kikugawa, T. Kako, S. Ouyang, H.S. Williams, H. Yang, J. Cao, Nat. Mater. 9 (2010) 559–564.
[16] S. Ouyang, H. Tong, N. Umezawa, J. Cao, P. Li, Y. Bi, Y. Zhang, J. Ye, J. Am. Chem. Soc. 134 (2012) 1974–1977.
[17] A. Kudo, Y. Miseki, Chem. Soc. Rev. 38 (2009) 253–278.
[18] S. Ouyang, J. Ye, J. Am. Chem. Soc. 133 (2011) 7757–7763.
[19] H. Zhou, X.F. Li, T.X. Fan, F.E. Osterloh, J. Ding, E.M. Sabio, D. Zhang, Q.X. Guo, Adv. Mater. 22 (2010) 951–956.
[20] X.F. Li, T.X. Fan, H. Zhou, S.K. Chow, W. Zhang, D. Zhang, Q.X. Guo, H. Ogawa, Adv. Func. Mater. 19 (2009) 45–56.
[21] R. Asahi, T. Morikawa, T. Ohwaki, K. Aoki, Y. Taga, Science 293 (2001) 269.
[22] S.U.M. Khan, M. Al-Shahry, W.B. Ingler, Science 297 (2002) 2243.
[23] D.A. Walker, Trends Plant Sci. 7 (2002) 183–185.
[24] A.J. Bard, J. Photochem. 10 (1979) 59.
[25] L. Ye, J. Liu, C. Gong, L. Tian, T. Peng, L. Zan, ACS Catal. 2 (2012) 1677–1683.
[26] K. Sayama, K. Mukasa, R. Abe, Y. Abe, H. Arakawa, J. Photochem. Photobiol. A 148 (2002) 71–77.
[27] X. Wang, G. Liu, L. Wang, Z. Chen, G.Q. Lu, H.M. Cheng, Adv. Energy Mater. 2 (2012) 42–46.
[28] K. Maeda, M. Higashi, D. Lu, R. Abe, K. Domen, J. Am. Chem. Soc. 132 (2010) 5858–5868.
[29] N. Fu, Z. Jin, Y. Wu, G. Lu, D. Li, J. Phys. Chem. C 115 (2011) 8586–8593.
[30] A. Iwase, Y.H. Ng, Y. Ishiguro, A. Kudo, R. Amal, J. Am. Chem. Soc. 133 (2011) 11054–11057.
[31] H. Lin, J. Cao, B. Luo, B. Xu, S. Chen, Catal. Commun. 21 (2012) 91–95.
[32] M. Higashi, R. Abe, T. Takata, K. Domen, Chem. Mater. 21 (2009) 1543.
[33] X. Wang, G. Liu, Z.-G. Chen, F. Li, L. Wang, G.Q. Lu, H.-M. Cheng, Chem. Commun. (2009) 3452.
[34] K. Sayama, K. Mukasa, R. Abe, Y. Abe, H. Arakawa, Chem. Commun. (2001) 2416.
[35] L. Zhang, K-H. Wong, Z. Chen, J.C. Yu, J. Zhao, C. Hu, C-Y. Chan, P-K. Wong, Appl. Catal. A, Gen. 363 (2009) 221–229.
[36] H. Tada, F. Suzuki, S. Ito, T. Akita, K. Tanaka, T. Kawahara, H. Kobayashi, J. Phys. Chem. B 106 (2002) 8714.
[37] H. Tada, T. Mitsui, T. Kiyonaga, T. Akita, K. Tanaka, Nat. Mater. 5 (2006) 702.
[38] V. Subramanian, E.E. Wolf, P.V. Kamat, J. Am. Chem. Soc. 126 (2004) 4943–4950.
[39] I. Honma, T. Sano, H. Komiyama, J. Phys. Chem. 97 (1993) 6692–6695.
[40] M. Murdoch, G.I.N. Waterhouse, M.A. Nadeem, J.B. Metson, M.A. Keane, R.F. Howe, J.L. Iorca, H. Idriss, Nat. Chem. 3 (2011) 489–492.
[41] A. Iwase, H. Kato, A. Kudo, Catal. Lett. 108 (2006) 7.
[42] M. Fujii, K. Nagasuna, M. Fujishima, T. Akita, H. Tada, J. Phys. Chem. C 113 (2009) 16711–16716.
[43] H. Zhu, B. Yang, J. Xu, Z. Fu, M. Wen, T. Guo, S. Fu, J. Zuo, S. Zhang, Appl. Catal. B, Environ. 90 (2009) 463–469.
[44] K. Kalyanasundaram, E. Borgarello, M. Gratzel, Helv. Chim. Acta 64 (1981) 362–366.
[45] H. Zhou, T.X. Fan, D. Zhang, ChemSusChem 4 (2011) 1344–1387.
[46] T.X. Fan, S-K. Chow, D. Zhang, Prog. Mater. Sci. 54 (2009) 542–659.